First publ. in: Journal of biomedical optics 10 (2005), 4, 044002

Non-Invasive Detection of Functional Brain Activity with Near-Infrared Diffusing-Wave Spectroscopy

J. Li,[1,2] G. Dietsche,[1] D. Iftime,[2] S. E. Skipetrov,[3] B. Rockstroh,[2] G. Maret,[1] T. Elbert,[2] and T. Gisler[1,*]

[1] *Universität Konstanz, Fachbereich Physik, 78457 Konstanz, Germany*

[2] *Universität Konstanz, Fachbereich Psychologie, 78457 Konstanz, Germany*

[3] *Laboratoire de Physique et Modélisation des Milieux Condensés/CNRS, Université Joseph Fourier, 38042 Grenoble, France*

Abstract

Near-infrared dynamic multiple scattering of light (diffusing-wave spectroscopy, DWS) is introduced as a new method for non-invasive measurement of functional brain activity in humans. DWS was used to detect activation of the somato-motor cortex in 11 right-handed volunteers who performed a finger opposition task separately with their right and with their left hand. Temporal autocorrelation functions $g^{(1)}(\tau)$ of the scattered light field were measured during 100 s periods of motor task alternating with 100 s resting baseline periods. Analyzing the experimental data with an analytical theory for $g^{(1)}(\tau)$ from a 3-layer geometry with optical and dynamical heterogeneity representing scalp, skull and cortex allowed to isolate the diffusion coefficient in cortical regions. During the motor task the cortical diffusion coefficient was found to be significantly increased, indicating enhanced activation-related dynamics in active cortical tissue. As expected from known brain hemispheric asymmetry for right-handed subjects the contralateral response was more pronounced than the ipsilateral response. These results suggest that near-infrared DWS can be used to non-invasively investigate subcellular dynamics in the cerebral cortex.

PACS numbers: 42.25.Fx; 42.66.-p; 87.57.-s; 87.62.+n; 87.64.-t; 87.80.-y.

Keywords: Non-invasive imaging, optical brain imaging, diffusing-wave spectroscopy.

INTRODUCTION

Optical methods have become increasingly important as diagnostic tools for non-invasive biomedical imaging since they offer great advantages to established methods such as positron emission tomography and magnetic resonance imaging in terms of portability, price and weakness of interaction (absence of radiation damage, etc.) [1–3]. In particular near-infrared light at wavelengths between around 750 nm and 950 nm provides significant advantages over visible or infrared light since absorption by the most abundant chromophores in tissue, such as melanin and hemoglobin, or water is weak, while at the same time scattering mean free paths are long enough that light can penetrate up to a few cm into tissue. However, the strong scattering of light is a generic obstacle to direct imaging of subsurface features in the body. It has its origin in the structural heterogeneities on the length scale of the wavelength of light. Rather than ballistic, light propagation deep inside tissue is diffusive, which strongly reduces the spatial resolution of optical imaging methods, in particular for structures deep within the body.

Several methods are currently used to extract, from the distribution of photon fluxes measured at the surface, information on subsurface *structures* with a scattering or absorption contrast: (i) time-of-flight experiments with gated detection allow for the discrimination of the early arriving ballistic photons and the reconstruction of optical density distributions [4]; (ii) low-coherence tomography operates in reflection and allows to enhance longitudinal spatial resolution down to several $10\,\mu$m many transport mean free paths below the surface [5]; (iii) frequency-domain imaging (often also called diffuse photon density wave imaging) uses a light source modulated at MHz frequencies and measures amplitude and phase of diffusely transmitted light that is detected some distance away from the source [6]. Frequency-domain imaging thus requires some means of calculating distributions of optical densities and absorption cross sections within the volume from an inversion of the measured data [7].

The frequency domain method has recently been applied to non-invasive *functional* imaging of cerebral activity after stimulation of specific brain areas such as the visual and motor cortices. Using a back-projection method low-resolution maps of cortical blood oxygenation following motor stimulation have been obtained with a temporal resolution of 160 ms [8–10]. These experiments show that the total hemoglobin concentration increases within about 4 s after the stimulation by up to 0.3 μM above its average level of about $70 - 80\,\mu$M. At much shorter times after stimulation (milliseconds), frequency-domain experiments have revealed small stimulus-related signal changes that are interpreted as an increase in the cortical turbidity [11, 12]. This fast optical signal had previously been observed in reflectance measurements on exposed cortical areas [13, 14]. Since the time scale of the fast optical signal is too short for significant optical changes due to increased blood flow, it is believed that it reflects the increased scattering from nerve cells following electrical activation, as has been directly observed in isolated neurons [15]. Increased activation-related scattering, in turn, is attributed to mechanisms such as cell swelling, increased concentration of vesicles, and ion density gradients [16].

Very recently it has been shown that even in the complete absence of scattering or absorption contrast information on dynamical heterogeneities within a turbid medium can be gained from spatially resolved measurements of the temporal autocorrelation function $g^{(2)}(\tau)$ of speckle intensities [17–19]. The mechanism for this novel imaging method is the one underlying diffusing-wave spectroscopy (DWS) used in colloid physics [20, 21]: multiply scattered photons undergo a phase shift due to the motion of scatterers, e.g. due to Brownian motion or laminar flow. When coherent light is used, the speckle pattern fluctuates with a characteristic correlation time which depends on the inherent dynamics of the scatterers and on the characteristic number of scattering events between source and detector. The temporal autocorrelation function of the scattered field is then given by

$$g^{(1)}(\tau) = \int_{l^*}^{\infty} P(s) \exp\left[-\frac{1}{3} k_0^2 \langle \Delta r^2(\tau) \rangle \frac{s}{l^*}\right] \mathrm{d}s \tag{1}$$

where $P(s)$ is the normalized distribution of photon path lengths s, $k_0 = 2\pi/\lambda$ is the wavenumber of light in the medium, and $\langle \Delta r^2(\tau) \rangle$ is the mean-squared displacement of scatterers within the time τ. The quantity l^* is the transport mean free path which is the step size of the photon's random walk. In the framework of the diffusion approximation using Eq. 1 is equivalent to solving the correlation-diffusion equation (see Eq. 4 in the Appendix), the latter having the advantage of being applicable to the case of complex geometries and spatially heterogeneous dynamics.

Unlike classical quasi-elastic light scattering (QELS) where $g^{(1)}(\tau)$ decays for displacements of $1/k_0$, the photon phase shift accumulated by many scattering events results in a decay of $g^{(1)}(\tau)$ for single-particle displacements $\Delta r \sim l^*/(sk_0)$ that are much smaller than the wavelength λ of light due to the long path length s. For $l^* = 1\,\mathrm{mm}$ and a source-receiver distance $L = 20\,\mathrm{mm}$ the average path length is roughly $L^2/l^* = 40\,\mathrm{cm}$. Hence multiple scattering conveys DWS an enhanced sensitivity to microscopic displacements within the turbid medium [22]. The fact that long photon paths give rise to the decay of $g^{(1)}(\tau)$ at short times (and, conversely, short paths to the long-time decay) provides DWS with a sort of coarse spatial resolution. In addition, the shape of the autocorrelation function is sensitive to the type of microscopic motion giving rise to speckle fluctuations, allowing, for instance, to discriminate laminar or shear flows from isotropic Brownian motion [23–25]. Enhanced perfusion of specific cortical areas due to neuronal activation should thus also lead to changes in the speckle dynamics observable in DWS.

However, experiments using the dynamic speckle contrast for brain imaging have been scarce: aiming at mapping blood flow velocities in cortical vessels, Lohwasser et al. have tried to account for the effects of multiple light scattering in laser Doppler spectra from brain phantoms [26]. Using a CCD camera, Dunn et al. [27] mapped the cerebral blood flow with spatially resolved measurements of the speckle contrast from an exposed rat cortex. A recent experiment by Cheung et al. [28] on a semi-exposed mouse brain revealed that the field autocorrelation function shows a faster decay upon stimulation by increased CO_2 partial pressure. This was interpreted as a signature of enhanced flow velocity of red blood cells in the cortical vessels. The measured field autocorrelation functions, however, showed a complex shape that could not be accounted for by predictions for simple diffusion or random flow. This suggests that using DWS to investigate functional brain activity in an entirely non-invasive way is likely to be complicated by the heterogenous optical and dynamical properties of the head consisting of scalp, skull, cerebrospinal fluid and white and gray matter. Model calculations of autocorrelation functions from optically and dynamically heterogeneous multilayer media based on the solution of the correlation-diffusion equation show a complicated decay of $g^{(1)}(\tau)$ which is not easily separated into contributions from the individual layers [29].

On the other hand, the scattering of light from subcellular organelles in cortical tissue should give rise to speckle fluctuations that are largely unrelated to blood flow. From isolated neural tissue it is known that neurosecretory release enhances the mobility of neurosynaptic vesicles [30–32], which might be detectable by DWS from intact cortical tissue. Activation of contralateral motor and sensory cortical regions by unimanual motor tasks [33–36] is a likely candidate for the detection of cortical activation by DWS since it is characterized by a large hemispherical asymmetry, in particular for right-handed subjects [37].

In this publication we use near-infrared DWS to detect functional activation of the human motor cortex through intact scalp and skull. Analyzing the measured DWS autocorrelation functions in terms of a 3-layer model allowing for different optical and dynamical parameters in the scalp, skull and cortex, we are able to separate the cortical dynamics from tissue optical parameters and scalp dynamics reflecting peripheral perfusion. For right-handed subjects, we find a significant increase of the cortical diffusion coefficient when a finger opposition task is performed. In accordance with the enhanced activation of the contralateral hand area of the primary somato-sensory and primary motor cortex by the finger opposition task, we find that the cortical diffusion coefficient for contralateral (right-hand) stimulation is significantly higher than the one for ipsilateral (left-hand) stimulation.

METHODS

Subjects

Eleven healthy adult volunteers (4 male, mean age 30.5 years, range 22-53 years) were recruited from students and faculty of the University of Konstanz. All subjects were right-handed as verified by a modified version of the Edinburgh Handedness Questionnaire [38]. The average score was 80-100; a 12th subject was discarded as left-handed. Prior to the experiment subjects were informed about the task and the measuring procedure and signed a written consent. The study protocol was appproved by the University's Ethical Review Board.

Task and procedure

During task and measurements the subject was sitting on a chair in a relaxed position and was asked to perform a finger opposition task with the right (dominant) hand. Task periods lasting 100 s each followed rest periods of 100 s during which the baseline data were recorded. Afterwards the sequence of baseline and task periods was repeated with the left hand. Subjects were asked to perform the finger opposition as fast and vigorously as possible, avoiding repetitive alternations. They were further instructed that they might imagine playing a piano or a violin, in order to increase the similarity to motor activation in real life.

Diffusing-wave spectroscopy

A diode laser operating at a wavelength $\lambda_0 = 802\,\mathrm{nm}$ (Toptica TA100) was coupled into a multi-mode optical fiber (core diameter 50 mm; numerical aperture 0.22) serving as an illuminating source. Multiply scattered light was collected by a few-mode optical fiber guiding about 6 transverse modes [39] at a distance of $20 - 25\,\mathrm{mm}$ from the source and detected with an avalanche diode operating in Geiger mode (Perkin-Elmer SPCM-AQR-15C). The intensity autocorrelation function $g^{(2)}(\tau) = \langle I(t)I(t+\tau)\rangle / \langle I(t)\rangle^2$ was then computed from the amplified and discriminated detector output by a digital multi-tau correlator (ALV5000E) at lag times between 200 ns and 3.1 s. Source and receiver fibers were mounted on a rigid fixation device which the subject could wear like a helmet. The intensity of the illuminating light was adjusted to be less than the maximum allowable intensity of $4\,\mathrm{mW/mm^2}$ [40]. Photon count rates high enough for computation of intensity autocorrelation functions within the stimulation period of 100 s were obtained by increasing both the incident laser power and the illuminated area on the scalp, thereby still keeping the peak intensity below the safety limit. This procedure was especially important for measurements on strongly pigmented subjects. The sensor, comprising light source and detector, was then fixed over the motor area on the left hemisphere (area C3 in the international 10-20 system [41] for electroencephalography (EEG)), (see Fig. 1). The direction from source to detector was arranged perpendicular to the direction of the central sulcus in order to facilitate the photon cloud to cross the area activated most by the motor task. Before fixing the source and detector, the hair was combed away so that the illuminator and detector had good optical contact to the scalp. During both the resting baseline and the task periods, each lasting 100 s, we recorded 10 normalized intensity autocorrelation functions, each with a duration of 10 s. In order to make sure that the amplitude of the measured intensity autocorrelation function was due to the few-mode receiver optics only (and not due to contributions of static scattering to the signal [42]), we measured $g^{(2)}(\tau)$ on a turbid latex sample immediately before and after the measurements on the subjects.

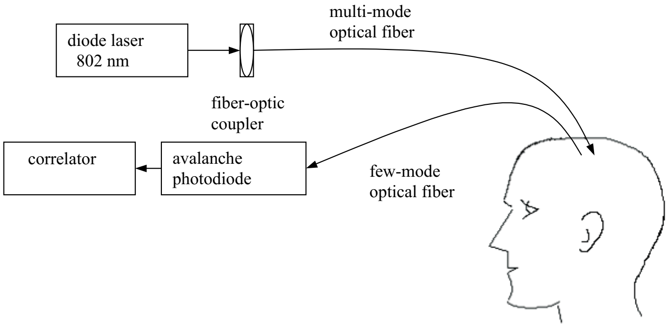

FIG. 1: Schematic diagram of the experimental setup. The receiver fiber collects and guides the multiply scattered light emitted from the scalp with a few transverse modes at the laser wavelength $\lambda_0 = 802\,\mathrm{nm}$.

Data analysis

We model the head by a simplified 3-layer geometry consisting of scalp (layer 1), skull (layer 2) and cortex (layer 3), each of them characterized by its thickness Δ, transport mean free path length l^*, absorption path length $l^{(\mathrm{a})}$ and diffusion coefficient D. Analytical expressions for the normalized field autocorrelation function $g^{(1)}(\tau) = \langle E^*(t)E(t+\tau)\rangle / \langle |E(t)|^2 \rangle$ obtained from the solution of the correlation-diffusion equation for this 3-layer model (see Appendix) were fitted to the measured intensity autocorrelation functions $g^{(2)}(\tau)$, using the Siegert relation [43]

$$g^{(2)}(\tau) = 1 + \beta_{\mathrm{coh}} \left| g^{(1)}(\tau) \right|^2 \tag{2}$$

between field and intensity autocorrelation functions. Using a Levenberg-Marquardt optimization routine yields the coherence factor β_{coh} and the diffusion coefficients D_1 and D_3 for the scalp and for the brain, respectively. The other parameters, such as the absorption length $l_n^{(\mathrm{a})}$, transport mean free path lengths l_n^* and the thickness of the scalp Δ_1 were treated as fixed parameters. For these quantities we used literature values [1, 44–46] $l_3^{(\mathrm{a})} = 25\,\mathrm{cm}$, $l_3^* = 0.57\,\mathrm{mm}$ for the human brain, $l_{1,2}^{(\mathrm{a})} = 2.5\,\mathrm{cm}$, $l_{1,2}^* = 1.0\,\mathrm{mm}$ for scalp and skull, and a scalp thickness $\Delta_1 = 3\,\mathrm{mm}$. We approximated the skull as a static medium (i.e. $D_2 = 0$), while its thickness is also determined by the fitting procedure.

Effects of activation were evaluated by comparing the diffusion coefficients measured during stimulation and during rest periods for both contralateral (right-hand) and ipsilateral (left-hand) stimulation by one-tailed t-tests.

RESULTS

Fig. 2 shows the reduced intensity autocorrelation functions $(g^{(2)}(\tau) - 1)/\beta_{\mathrm{coh}}$ from a selected subject obtained from the left hemisphere (C3) during baseline and activation, respectively. Data are averages over 2 blocks of 10 runs each. The autocorrelation function recorded during contralateral stimulation shows a significantly faster decay than during the resting baseline period. Modelling the autocorrelation function by the solution of the correlation-diffusion equation for a semi-infinite 1-layer geometry, assuming free diffusion as the mechanism for speckle decorrelation, gave rather poor agreement with the experimental data. Modelling the dynamics by a random flow $\langle \Delta r^2(\tau) \rangle = \langle v^2 \rangle \tau^2$ with a Gaussian flow

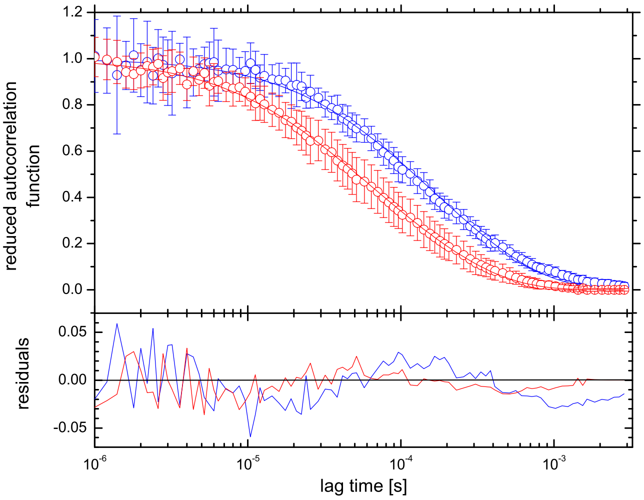

FIG. 2: Reduced intensity autocorrelation function $(g^{(2)}(\tau)-1)/\beta_{\rm coh}$ measured over the C3 area of the motor cortex of a right-handed subject for a source-receiver distance of 20 mm. The blue circles are the resting baseline data; the red circles are the data for contralateral stimulation. The error bars are standard deviations from 2 blocks of 10 runs each. Lines are fits of the analytical solution of the 3-layer correlation-diffusion equation 4 to the data. Best-fit values for diffusion coefficients D_1 and D_3 of scalp and cortex, respectively, are $D_1 = 2.3\times10^{-9}{\rm cm}^2/{\rm s}$ and $D_3 = 3.1\times10^{-9}{\rm cm}^2/{\rm s}$ for the resting baseline period and $D_1 = 4.0\times10^{-9}{\rm cm}^2/{\rm s}$ and $D_3 = 8.8\times10^{-9}{\rm cm}^2/{\rm s}$ for the stimulation period.

velocity v yielded, due to the increased curvature of $g^{(1)}(\tau)$, even poorer agreement than the free diffusion model. These discrepancies are resolved when we use the solution of the correlation-diffusion equation 4 for a 3-layer medium, representing the scalp by a finite layer with a thickness $\Delta_1 = 3\,\mathrm{mm}$, and the cortex as the innermost, semi-infinite layer. With this dynamic 3-layer model the fitting procedure yields a cortical diffusion coefficient $D_3 = 3.1 \times 10^{-9}\mathrm{cm}^2/\mathrm{s}$ during the resting period and $D_3 = 8.8 \times 10^{-9}\mathrm{cm}^2/\mathrm{s}$ during the stimulation period. The best-fit value $\Delta_2 = 4.6\,\mathrm{mm}$ for the skull thickness obtained from the DWS data was, to within experimental error, identical for both baseline and stimulation data. Although the skull was modelled as a completely static layer, its incorporation was found to be necessary to account for the decay of the autocorrelation function at intermediate times. The decay of the autocorrelation function at long times is dominated by the scalp diffusion coefficient D_1 which is found to increase with stimulation (see below). Both for resting and stimulation periods the model slightly underestimates the autocorrelation function at the longest lag times, as can be seen from the residuals (Fig. 2). This might be due to the omission of the very weakly scattering cerebrospinal fluid (CSF) layer in our model of the head. We expect that reflections at the boundaries of the CSF layer [45] will lead to a slightly larger weight of short photon paths, which in turn would lead to an amplitude in $g^{(1)}(\tau)$ at long times which is slightly higher than predicted by the 3-layer model. Nevertheless the overall agreement between theory and experiment is very good given the complex shape of the correlation function. When measuring the autocorrelation function after the end of the motor task, the correlation functions were found to be identical with the baseline correlation functions before stimulation. Analyzing individual autocorrelation functions recorded over 10 s each yields information on the distribution of the fitting parameters Δ_2, D_1 and D_3. Due to the limited photon statistics and the decay times in the 0.1 ms range individual autocorrelation functions are noisier than the averaged autocorrelation function. Nevertheless, the fitting routine converges, and, using a fixed skull thickness $\Delta_2 = 4.6\,\mathrm{mm}$ the average best-fit values $D_1 = (2.5 \pm 0.8) \times 10^{-9}\mathrm{cm}^2/\mathrm{s}$ and $D_3 = (3.2 \pm 1.5) \times 10^{-9}\mathrm{cm}^2/\mathrm{s}$ for the baseline and $D_1 = (5.8 \pm 2.5) \times 10^{-9}\mathrm{cm}^2/\mathrm{s}$ and $D_3 = (6.8 \pm 2.3) \times 10^{-9}\mathrm{cm}^2/\mathrm{s}$ for stimulation agree well with the diffusion coefficients obtained from fitting the averaged data. Furthermore this analysis shows that the differences in D_3 and D_1 upon motor stimulation observed in the averaged autocorrelation functions is indeed significant.

When the stimulation is exerted by the left hand, ipsilateral to C3, the autocorrelation function recorded from C3 is found to decay significantly more slowly than for contralateral stimulation (see Fig. 3). This slower decay is mainly due to fact that the cortical diffusion coefficient for contralateral stimulation $D_3 = 8.8 \times 10^{-9}\mathrm{cm}^2/\mathrm{s}$ is larger than the one for ipsilateral stimulation, $D_3 = 6.3 \times 10^{-9}\mathrm{cm}^2/\mathrm{s}$. In contrast, the scalp diffusion coefficients are not significantly different between ipsilateral and contralateral stimulation, although they both are increased with respect to the value for the resting period.

Autocorrelation functions obtained from the 11 subjects taken during resting and stimulation periods showed an equally good agreement with the prediction of the correlation-diffusion theory. However, the absolute values of the cortical diffusion coefficients vary over a large range, both for the resting and for the stimulation periods (see Fig. 4). Still, the finger opposition task produces a significant increase in the cortical diffusion coefficient D_3 detected at C3 during contralateral stimulation (t-test (1-tailed): $p = 0.01 < 0.05$), as shown in Fig. 4. In contrast, ipsilateral (left hand) stimulation did not result in a significant increase in D_3 (t-test (1-tailed): $p = 0.10 > 0.05$). Across the subjects, baseline cortical diffusion coefficients recorded prior to contralateral stimulation are indistinguishable from the ones measured prior to ipsilateral stimulation (t-test (2-tailed): $p = 0.33 \gg 0.05$). This implies that the cortical diffusion coefficients for contralateral stimulation are indeed significantly higher than for ipsilateral stimulation across the subject group (t-test (1-tailed): $p = 0.04 < 0.05$).

The effect of the finger opposition task on the scalp diffusion coefficient D_1 is less clear-cut than in the case of the cortical diffusion coefficient: contralateral stimulation leads to a small but significant increase in D_1 above the baseline value (t-test (1-tailed): $p = 0.01 < 0.05$), while no such an increase can be seen for ipsilateral stimulation (t-test (1-tailed): $p = 0.10 > 0.05$). This is in contrast to what would be expected assuming that an enhanced D_1 is due to peripheral perfusion which should not distinguish between hemispheres. Closer inspection of the data shows that the origin of this asymmetry can be traced back to an difference in the baseline values of D_1 measured immediately before contra- and ipsilateral stimulation which is yet unexplained. Support for the hypothesis that finger opposition also enhances the peripheral blood flow is provided by the observation that the DWS autocorrelation function from a subject's right lower arm is found to decay faster while performing finger opposition with the left hand.

In our experiments with the 11 subjects, in 2 subjects the DWS response to ipsilateral

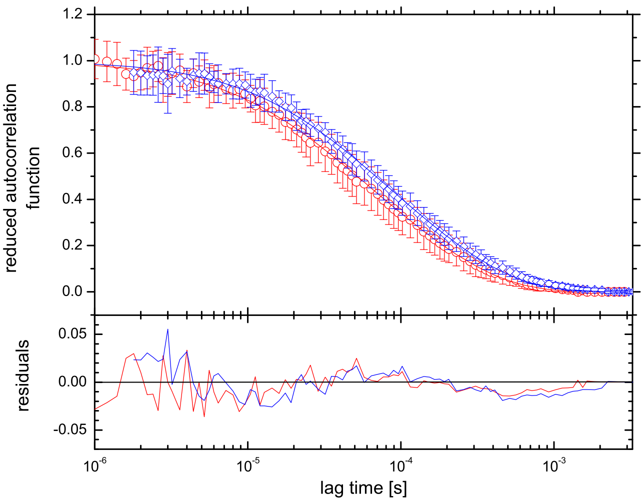

FIG. 3: Reduced intensity autocorrelation function $(g^{(2)}(\tau) - 1)/\beta_{\mathrm{coh}}$ measured over the C3 area of the motor cortex of a right-handed subject for a source-receiver distance of 20 mm. The blue diamonds are the data for ipsilateral (left-hand) stimulation; the red circles are the data for contralateral stimulation. The error bars are standard deviations from 2 blocks of 10 runs each. Lines are fits of the analytical solution of the 3-layer correlation-diffusion equation 4 to the data. Best-fit values for diffusion coefficients D_1 and D_3 of scalp and cortex, respectively, are $D_1 = 3.4 \times 10^{-9}\mathrm{cm}^2/\mathrm{s}$ and $D_3 = 6.3 \times 10^{-9}\mathrm{cm}^2/\mathrm{s}$ for ipsilateral stimulation and $D_1 = 4.0 \times 10^{-9}\mathrm{cm}^2/\mathrm{s}$ and $D_3 = 8.8 \times 10^{-9}\mathrm{cm}^2/\mathrm{s}$ for the contralateral stimulation.

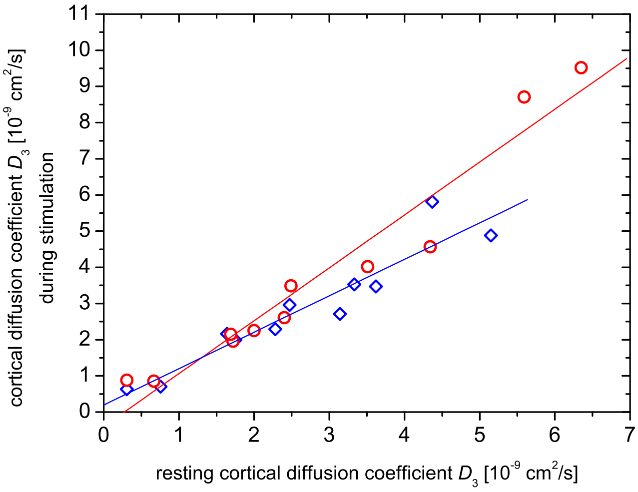

FIG. 4: Cortical diffusion coefficients D_3 from the C3 motor area of 11 right-handed subjects, for contralateral (red circles) and for ipsilateral (blue diamonds) stimulation, as a function of the diffusion coefficients measured during the resting baseline periods. Contralateral stimulation (red circles) shows a significant increase in D_3 over the value during the baseline resting period, as shown by a 1-tailed t-test ($p = 0.01 < 0.05$). In contrast, no significant enhancement of the dynamics is seen for ipsilateral stimulation (t-test (1-tailed): $p = 0.10 > 0.05$). The lines are linear least-squares fits to the function $D_{3,\,\mathrm{stimulation}} = a + bD_{3,\,\mathrm{baseline}}$, yielding slopes $b = 1.46 \pm 0.12$ for contralateral and $b = 1.01 \pm 0.11$ for ipsilateral stimulation; intercepts a vanish to within statistical error. Direct comparison of D_3 for contralateral and ipsilateral stimulation shows a significant asymmetry in the response of the cortical diffusion coefficient D_3 upon motor stimulation (t-test (1-tailed): $p = 0.04 < 0.05$).

stimulation is larger than the one to contralateral stimulation, opposite to what would be expected from EEG data. This anomaly might result from a variant in the location of the contralateral somato-motor hand representation that may not be near the C3-scalp location in these subjects, or from an anomaly in the motor organization which is known to occur in about 5% of the subjects [36].

DISCUSSION

As the theoretical expression (Eqs. 18–19) for the 3-layer model used for extracting cortical and scalp diffusion coefficients depends on 10 parameters (layer thickness $\Delta_{1,2}$, absorption path lengths $l^{(\mathrm{a})}_{1,2,3}$, transport mean free path lengths $l^{*}_{1,2,3}$ and diffusion coefficients $D_{1,3}$) when the skull is treated as a static medium, it is important to know how robust the determination of D_3, D_1 and Δ_2 is with respect to the uncertainty in the optical parameters $l^{(\mathrm{a})}_{n}$ and l^{*}_{n} of scalp, skull and cortex and in the local thickness of the skin. In particular an uncontrolled increase in the cortical transport mean free path could be interpreted as an decreased cortical diffusion coefficient. Conversely, a decrease in the cortical absorption coefficient could be interpreted as an increase of the diffusion coefficient. Weaker influences on the determination of the cortical diffusion coefficient are expected from changes in the optical properties of the scalp and skull, since these affect the decay of the autocorrelation function at long times. We have thus modelled autocorrelation functions with largely varying values of the optical and dynamical parameters using the analytical solution of the correlation-diffusion equation for a 3-layer model of the human head, and compared these predictions with measured data. Fig. 5a shows a plot of the square root of the sum of squared residuals,

$$\chi = \left[\sum_{i=1}^{N} \left(y_i - g(\tau_i; \Delta_{1,2}, l^{(\mathrm{a})}_{1,2,3}, l^{*}_{1,2,3}, D_{1,3}) \right)^2 \right]^{1/2} \tag{3}$$

between experimental baseline data $y_i \equiv g^{(2)}(\tau_i)$ and the calculated raw intensity correlation function $g(\tau_i; \Delta_{1,2}, l^{(\mathrm{a})}_{1,2,3}, l^{*}_{1,2,3}, D_{1,3})$ as a function of D_3 and $l^{(\mathrm{a})}_{3}$. We have varied the cortical absorption length from $l^{(\mathrm{a})}_{3} = 12.5\,\mathrm{cm}$ to $l^{(\mathrm{a})}_{3} = 50.0\,\mathrm{cm}$, around the literature value $l^{(\mathrm{a})}_{3} = 25.0\,\mathrm{cm}$, and the cortical diffusion coefficient from $D_3 = 1.5 \times 10^{-9}\mathrm{cm}^2/\mathrm{s}$ to $D_3 = 6.6 \times 10^{-9}\mathrm{cm}^2/\mathrm{s}$, around the best-fit value $D_3 = 3.1 \times 10^{-9}\mathrm{cm}^2/\mathrm{s}$ obtained from the averaged data using the literature values for optical parameters cited above. We find that χ shows a pronounced minimum at the best-fit value $D_3 = 3.1 \times 10^{-9}\mathrm{cm}^2/\mathrm{s}$ and the literature value $l_3^{(\mathrm{a})} = 25.0\,\mathrm{cm}$. However, fits with only slightly higher χ could be obtained by increasing D_3 and reducing $l_3^{(\mathrm{a})}$. The coupling of $l_3^{(\mathrm{a})}$ and D_3 reflects the fact that higher absorption cuts off long photon paths, which in turn might be interpreted as a slowed-down dynamics. Such an underestimation of D_3 can occur if the data quality is not sufficient to capture the rounding of $g^{(1)}(\tau)$ at short lag times which is the hallmark of absorption. However, bounds for the activation-related changes in $l_3^{(\mathrm{a})}$ can be obtained from independent measurements using frequency-domain or time-of-flight methods. Recent experiments show that the concentration of deoxy-hemoglobin in the motor cortex decreases upon activation by up to about $0.2\,\mu\mathrm{M}$, while the increased oxygen consumption is reflected by an increase of the oxy-hemoglobin concentration by about $0.6\,\mu\mathrm{M}$ [10] over the average total hemoglobin concentration of about $74\,\mu\mathrm{M}$. At the wavelength $\lambda_0 = 802\,\mathrm{nm}$ used in our experiments which is close to the isosbestic point of oxy-/deoxy-hemoglobin, changes in the cortical absorption coefficient $1/l_3^{(\mathrm{a})}$ are thus expected to be proportional to changes in the total hemoglobin concentration which are of the order of 10^{-2} around the baseline level. From our sensitivity plot, however, such changes would lead to changes in the cortical diffusion coefficient of no more than a few percent.

On the other hand, a plot of χ as a function of D_3 and l_3^* (see Fig. 5b) shows again that the minimum of χ around the optimal fit parameter $D_3 = 3.1 \times 10^{-9}\mathrm{cm}^2/\mathrm{s}$ is quite pronounced. Increasing the cortical transport mean free path length l_3^* to $l_3^* = 0.12\,\mathrm{cm}$ leads to a second minimum in χ. Are realistic activation-related and hemodynamic changes in l_3^* large enough that the fitting procedure could be biased into the second minimum with a larger diffusion coefficient? As shown by recent frequency-domain experiments [12], the amplitude of the fast optical signal associated with activation-related changes in l_3^* are of the order of 10^{-4}, much too small to bias the estimation of D_3 away from the best-fit value $D_3 = 3.1 \times 10^{-9}\mathrm{cm}^2/\mathrm{s}$. The second mechanism that can lead to changes in l_3^* is the change in cortical blood volume associated with pulsation. Both mechanisms lead to enhanced light scattering by blood cells. The amplitude of activation-related modulation of cerebral blood volume is not precisely known at present, but the estimate based on the activation-related absorption changes indicates that the associated change in l_3^* should be of the order of 0.8%. In turn, pulsation-related blood volume changes increase the transmitted intensity by about 6% [47], indicating that the associated modulation of l_3^* is about as much. Furthermore, as the integration time of our experiment comprises about 10 pulsation

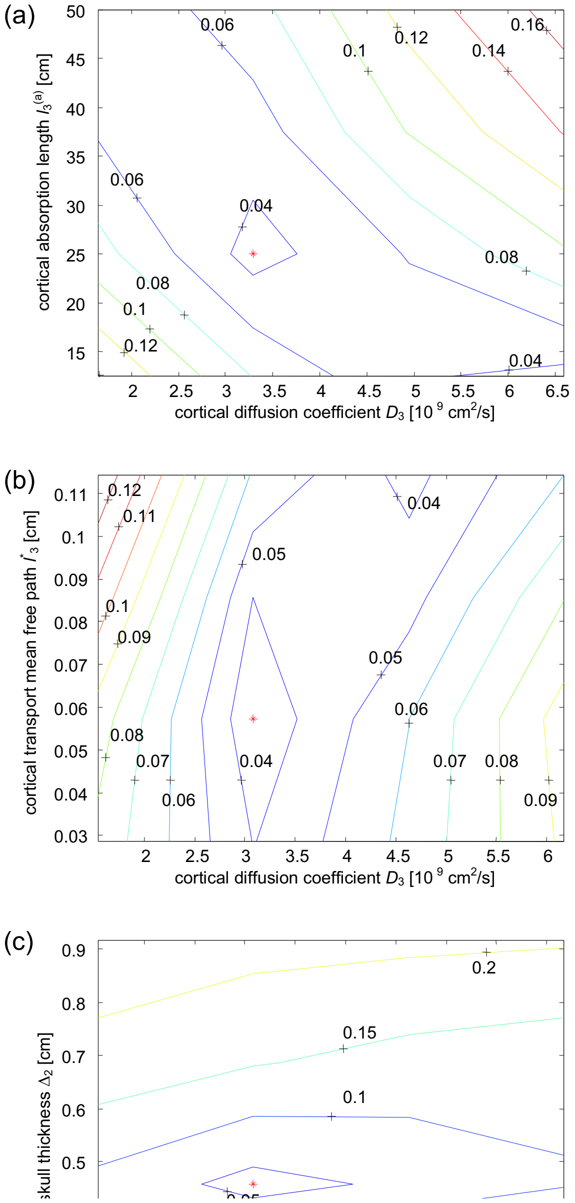

FIG. 5: Plot of χ between the prediction of the correlation-diffusion equation for a 3-layer model (Eq. 4) and experimental baseline data as a function of cortical diffusion coefficient D_3 and cortical absorption length $l_3^{(a)}$ (a), cortical transport mean free path length l_3^* (b), and skull thickness Δ_2 (c). Parameters for the calculation are $l_1^{(a)} = 2.5\,\text{cm}$, $l_1^* = 0.1\,\text{cm}$, $\Delta_1 = 0.3\,\text{cm}$ for the scalp; $l_2^{(a)} = 2.5\,\text{cm}$, $l_2^* = 0.1\,\text{cm}$, $\Delta_2 = 0.458\,\text{cm}$ for the skull; $l_3^{(a)} = 25\,\text{cm}$, $l_3^* = 0.0571\,\text{cm}$, $\Delta_3 = \infty$ for the cortex. Diffusion coefficients are $D_1 = 2.3 \times 10^{-9}\text{cm}^2/\text{s}$ for the scalp, $D_2 = 0$ for the skull, and $D_3 = 3.1 \times 10^{-9}\text{cm}^2/\text{s}$ for the brain. The asterisks mark the minimum of χ.

periods, we average over pulse-induced modulations of l_3^*. The third mechanism responsible for large turbidity changes in cerebral tissue is the $0.1\,\mathrm{Hz}$ vasomotoric reflectance signal superimposed on pulsation [48] which is characterized by changes in the transport mean free path of up to 2%. Combined with the observation that the pulse rate does not change between resting and task periods we conclude that the uncertainty in l_3^* is of the order of 8%, which is too small to bias the fitting routine into the χ minimum at the larger diffusion coefficient $D_3 \approx 4.6 \times 10^{-9}\mathrm{cm}^2/\mathrm{s}$. From these considerations we conclude that the determination of D_3 is indeed robust against realistic uncertainties in l_3^*.

The shape of the cross-over from the short-time decay to the long-time decay in $g^{(1)}(\tau)$ is dominated by the thickness Δ_2 of the skull which we approximate as a static turbid medium. The plots of χ as a function of Δ_2 and D_3 (Fig. 5c) and as a function of Δ_2 and D_1 (Fig. 6a) show that the skull thickness can be determined from the fit with good accuracy almost independently from the diffusion coefficients of brain and scalp, D_3 and D_1, respectively.

The long-time decay of $g^{(1)}(\tau)$ is dominated by the short photon paths that travel mainly through the scalp. Here the plot of χ vs. D_1 and $l_1^{(\mathrm{a})}$ (Fig. 6b) shows a weaker correlation than for the analogous brain parameters. This might be due to the larger systematic deviations between experiment and theory at long times which washes out the expected anticorrelation between absorption length and diffusion coefficient.

The plot of χ vs. D_1 and l_1^* (see Fig. 6c) shows a single minimum with a weak gradient in the D_1 direction. Here D_1 can vary by almost 50% above or below the optimal value $D_1 = 2.3 \times 10^{-9}\mathrm{cm}^2/\mathrm{s}$ before the quality of the fit is significantly reduced, whereas under- or overestimation of l_1^* will quickly lead to a higher χ. This insensitivity in the determination of D_1 can be overcome by measuring $g^{(1)}(\tau)$ at smaller source-receiver distances.

Finally, the dependence of χ on D_1 and D_3 (Fig. 7) shows a single minimum. This means that the correct estimation of D_3 is strongly coupled to an optimal value of D_1. Here the coupling of D_3 and D_1 reflects the fact that an overestimation of D_3 away from the optimal value $D_3 = 3.1 \times 10^{-9}\mathrm{cm}^2/\mathrm{s}$ can be partially compensated by an underestimated D_1 in order to keep χ acceptably low. However, as the short-time decay is dominated by D_3 and the long decay times mainly reflect superficial dynamics, grossly under- or overestimated D_1 or D_3 will appear in a shape of $g^{(1)}(\tau)$ that cannot be superimposed with the measured data.

It should be noted that the same qualitative behavior is shown when χ is calculated between theory and experimental data recorded during stimulation.

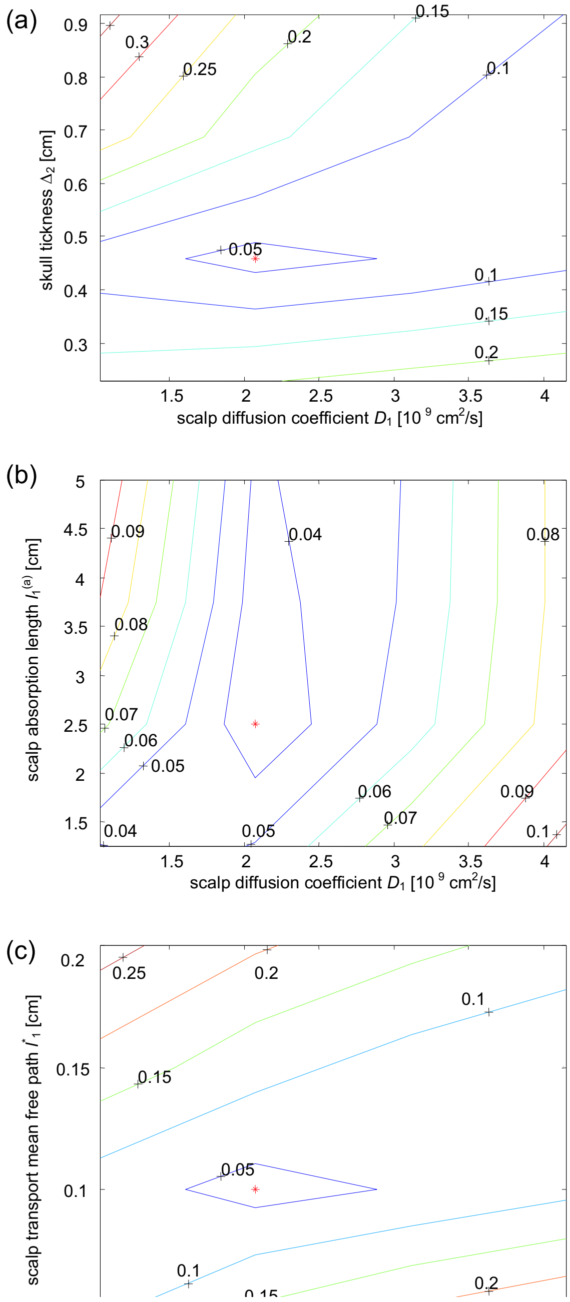

FIG. 6: Plot of χ between the prediction of the 3-layer correlation-diffusion theory and the experimental baseline data as a function of scalp diffusion coefficient D_1 and skull thickness Δ_2 (a), scalp absorption length $l_1^{(a)}$ (b), and scalp transport mean free path length l_1^* (c). Constant parameters are as in Fig. 5.

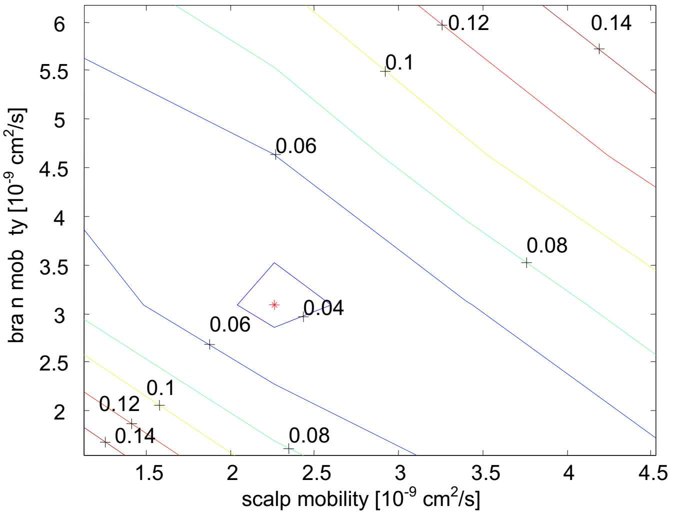

FIG. 7: Plot of χ between the prediction of the 3-layer correlation-diffusion theory and the experimental baseline data as a function of the diffusion coefficients D_1 and D_3 of scalp and cortex, respectively. Constant parameters are as in Fig. 5.

In addition from the considerations on the robustness of the fitting procedure with respect to uncertainties in optical parameters, the accuracy in determining cortical diffusion coefficients also depends on the noise in the measured data arising from finite photon counting statistics. Noise in correlation functions is itself correlated and difficult to estimate [49]. In general, autocorrelation functions measured with low average photon count rate or fast decay times are particularly prone to errors. In order to assess the variance of D_3 arising from noise in the data, we analyzed the data for subject 3. These data show both a low average count rate of 21 kHz, and a short average decay time $\overline{\tau} = 38\,\mu$s [52]. Analyzing the 10 autocorrelation functions individually with fixed coherence factor $\beta_{\mathrm{coh}} = 0.075$ [53] and fixed skull thickness $\Delta_2 = 5.1\,$mm yielded cortical diffusion coefficients $D_3 = (6.5 \pm 2.4) \times 10^{-9}\mathrm{cm}^2/\mathrm{s}$ during the resting baseline period and $D_3 = (9.1 \pm 1.1) \times 10^{-9}\mathrm{cm}^2/\mathrm{s}$ for contralateral stimulation. These values are in good agreement with the ones obtained from the analysis of the averaged autocorrelation functions (see Fig. 4). The analysis of these data shows that with even considerable noise in the measured data, the difference in cortical diffusion coefficients between resting baseline and stimulation periods is highly significant within the data sets from a single subject, at least for contralateral stimulation where the somato-sensory activation can be expected to be maximal.

Clearly our analysis of the sensitivity of the fitting procedure on uncertainties in the optical and dynamical parameters shows that within realistic bounds for the optical and dynamical tissue parameters the faster decay of the autocorrelation function during a motor task can be assigned to an increase in cortical diffusion coefficient due to cortical activation. It is, however, not quite clear whether this enhanced dynamics is due to blood flow or due to neuronal dynamics, or due to a combination of both. Red blood cells flowing through vessels are known to show a complicated, shear-rate dependent behavior, including the formation of rouleaux, which could affect the spectrum of their shape fluctuations during activation-related vasodilation. This in turn might speed up the speckle dynamics observed in DWS. On the other hand quasi-elastic light scattering experiments on isolated lobster and crab pericardial organs indicate that synaptic vesicles become more mobile upon neurosecretory release [30–32], possibly due to a partial depolymerization of the cytoskeleton. This increased vesicle mobility should then be reflected in a larger cortical diffusion coefficient D_3 in the DWS data. Interestingly, the diffusion coefficients obtained in our DWS experiments during stimulation agree to within a factor of 0.8 with the ones of synaptic particles observed by

Sattelle et al. [31].

With the current motor stimulation protocol we used in our experiments, it is however not possible to determine the origin of the short-time decay of the autocorrelation function unambiguously. One possible way to answer this question is by measuring the temporal intensity autocorrelation function with a shorter integration time. If the signal is due to cerebral hemodynamics, the maximum difference of D_3 (compared with the baseline measurement) should appear with a delay of several seconds with respect to the onset of stimulation. In contrast, if some kind of neurotransmitter motions also make a significant contribution to the DWS signal, one should detect signals earlier, from several tens to hundreds of milliseconds after the beginning of neuronal activation. In order to address this question experimentally, we plan to use our visual stimulation protocol with rapid visual serial presentation [50]. The high temporal resolution of EEG and magnetoencephalography (MEG) revealed that the brain is capable of switching rapidly (within less than 100 ms) between stimuli, recognizing the emotional character of each input picture. Obviously the cerebral blood flow cannot follow such rapid changes, so if other fast dynamical process, such as neurotransmitter motion, also contributes significantly to the DWS signal, distinct signal changes for high-arousing versus low-arousing affective stimuli over parietal (preferably right-hemispheric) areas should be seen with this technique.

CONCLUSIONS

We have shown that diffusing-wave spectroscopy can be used to detect brain functional activity in humans during motor stimulation in an entirely non-invasive way. Measured temporal autocorrelation functions of near-infrared laser light transmitted diffusely through the human head are analyzed using the analytical solution of the correlation-diffusion equation for a 3-layer geometry modelling the human head. The 3-layer theory allows to obtain good agreement with the experimental data over the entire range of lag times, and yields a quantitative estimate for the cortical diffusion coefficient. Analyzing the sensitivity of the model to uncertainties in tissue optical parameters and thicknesses we find that the cortical diffusion coefficient can be extracted from our data to within a few percent if we allow tissue optical parameters to vary within realistic bounds. Performing motor stimulation experiments on 11 right-handed subjects, the autocorrelation function from the C3 region is found to decay faster during the stimulation period. This enhancement of the dynamics is shown to arise from changes in the cortical dynamics and not from changes in the optical properties of the tissue. The marked hemispheric asymmetry between the measured cortical diffusion coefficients in the C3 region for left- and for right-hand stimulation is consistent with the dominant activation of the contralateral motor and sensory regions by unimanual motor tasks.

Our results suggest that advanced analysis of autocorrelation functions, improved photon counting statistics and the combination with frequency-domain tomography to measure tissue optical properties independently [51] might turn DWS into a powerful method for the investigation of functional brain activities, such as evoked by auditory and visual stimuli, as well as other mental tasks.

We acknowledge A. Wille for experimental work in the early stages of the project. This work was funded by the Optik-Zentrum Konstanz and by the Zentrum für Wissenschaftlicher Nachwuchs at the University of Konstanz.

APPENDIX: FIELD AUTOCORRELATION FUNCTION FROM AN N-LAYER TURBID MEDIUM

We consider a turbid medium consisting of N slabs with parallel boundaries located at depths $z = L_n$ ($n = 1, \ldots, N$). The front surface of the medium is located at $z = L_0 = 0$. Each slab with thickness $\Delta_n = L_n - L_{n-1}$ is characterized by its transport mean free path l_n^* and absorption length $l_n^{(\mathrm{a})}$ ($n = 1, \ldots, N$). For each slab, we assume its thickness Δ_n to be much larger than the respective transport mean free path l_n^*. Scatterer dynamics inside each layer is modelled by a diffusion coefficient D_n. Unlike the treatment for DWS from a multilayer system given in [29], we here assume that the source of monochromatic light is point-like, located at $\boldsymbol{r}' = \{\boldsymbol{\rho}' = 0, z'\}$ inside the first layer.

In the diffusion approximation, the normalized temporal autocorrelation function of the scattered field, $g^{(1)}(\boldsymbol{r}, \tau)$ is obtained from the the correlation-diffusion equation [19, 24]

$$\left[\nabla^2 - \alpha^2(\tau)\right] G(\boldsymbol{r}, \tau) = -s_0 \delta(\boldsymbol{r} - \boldsymbol{r}') \tag{4}$$

for the *unnormalized* field autocorrelation function $G(\boldsymbol{r}, \tau) = \langle E^*(\boldsymbol{r}, 0) E(\boldsymbol{r}, \tau) \rangle$. In each layer the loss of correlation due to the motion of the scatterers is given by

$$\alpha_n^2(\tau) = \frac{3}{l_n^* l_n^{(\mathrm{a})}} + \frac{6\tau}{\tau_n^{(0)} {l_n^*}^2} \tag{5}$$

where $\tau_n^{(0)} = (k_n^2 D_n)^{-1}$ is the single-scattering correlation time and k_n is the wavenumber of the light in the n-th layer.

Eq. 4 is conveniently solved using the Fourier transform of $G(\boldsymbol{r}, \tau)$ with respect to the transverse coordinate $\boldsymbol{\rho}$

$$\hat{G}(\boldsymbol{q}, z, \tau) = \int \mathrm{d}^2\boldsymbol{\rho}\, G(\boldsymbol{r}, \tau) e^{i\boldsymbol{q}\boldsymbol{\rho}} \tag{6}$$

yielding

$$\left[\frac{\partial^2}{\partial z^2} - \beta^2(\boldsymbol{q}, \tau)\right] \hat{G}(\boldsymbol{q}, z, \tau) = -s_0 \delta(z - z') \tag{7}$$

for $\hat{G}(\boldsymbol{q}, z, \tau)$. Here $\beta_n^2(\boldsymbol{q}, \tau) = \alpha_n^2(\tau) + \boldsymbol{q}^2$.

We divide the first layer in two 'sub-layers': layer '0' ($0 < z < z'$), identified by $n = 0$, and layer '1' ($z' < z < L_1$), identified by $n = 1$ in the following. The solution of Eq. 7 inside the n-th layer ($n = 0, 1, 2, \ldots, N$) then can be written as

$$\hat{G}_n(\boldsymbol{q}, z, \tau) = A_n e^{\beta_n z} + B_n e^{-\beta_n z} \tag{8}$$

where A_n and B_n are constant (i.e. z-independent) factors which are obtained from the boundary conditions

$$\hat{G}_0(\boldsymbol{q}, z, \tau) - z_0 \frac{\partial}{\partial z} \hat{G}_0(\boldsymbol{q}, z, \tau) = 0, \qquad z = 0 \tag{9}$$

$$\hat{G}_0(\boldsymbol{q}, z, \tau) = \hat{G}_1(\boldsymbol{q}, z, \tau), \qquad z = z' \tag{10}$$

$$\frac{\partial}{\partial z} \hat{G}_0(\boldsymbol{q}, z, \tau) = \frac{\partial}{\partial z} \hat{G}_1(\boldsymbol{q}, z, \tau), \qquad z = z' \tag{11}$$

$$\hat{G}_n(\boldsymbol{q}, z, \tau) = \hat{G}_{n+1}(\boldsymbol{q}, z, \tau), \qquad z = L_n, \quad n = 1, \ldots, N-1 \tag{12}$$

$$\mathcal{D}_n \frac{\partial}{\partial z} \hat{G}_n(\boldsymbol{q}, z, \tau) = \mathcal{D}_{n+1} \frac{\partial}{\partial z} \hat{G}_{n+1}(\boldsymbol{q}, z, \tau), \qquad z = L_n, \quad n = 1, \ldots, N-1 \tag{13}$$

$$\hat{G}_N(\boldsymbol{q}, z, \tau) + z_L \frac{\partial}{\partial z} \hat{G}_N(\boldsymbol{q}, z, \tau) = 0, \qquad z = L_N \tag{14}$$

where $z_0 \sim l_1^*$ and $z_L \sim l_N^*$ are the extrapolation lengths taking into account internal reflections at the external ($z = 0$ and $z = L_N$, respectively) boundaries of the slab. $\mathcal{D}_n = c l_n^*/3$ denotes the photon diffusion coefficient in layer n, and c is the speed of light.

When Eq. 8 is substituted into Eqs. (9)–(14), we obtain a system of $2(N+1)$ linear algebraic equations for coefficients A_n, B_n ($n = 0, 1, \ldots, N$). The Fourier transform $\hat{G}_0(\boldsymbol{q}, z = 0, \tau)$ of the autocorrelation function of diffusely reflected light $G_0(\boldsymbol{r}, \tau)$ measured at the front surface of the slab is then obtained by substituting the resulting A_0, B_0 into Eq. 8. In all cases, $\hat{G}_0(\boldsymbol{q}, z = 0, \tau)$ can be expressed as

$$\hat{G}_0(\boldsymbol{q}, z = 0, \tau) = \frac{\text{numerator}}{\text{denominator}} \tag{15}$$

We now give explicit expressions for the numerator and the denominator in Eq. 15 for a semi-infinite 1-layer medium and our 3-layer head model (scalp, skull and cortex). As a reasonable approximation, in our calculation we consider the third layer (cortex) as a semi-infinite medium.

For the case of a semi-infinite 1-layer medium Eqs. 8–14 yield

$$\begin{aligned} \text{numerator} &= s_0 z_0 e^{-\beta z'} &(16)\\ \text{denominator} &= 1 + \beta z_0 &(17) \end{aligned}$$

The analogous solution for the case of a 3-layer medium with an infinitely thick third layer $\Delta_3 \to \infty$ yields

$$\begin{aligned} \text{numerator} &= s_0 z_0 \left(\beta_1 \mathcal{D}_1 \cosh(\beta_1 (\Delta_1 - z'))\, (\beta_2 \mathcal{D}_2 \cosh(\beta_2 \Delta_2) + \beta_3 \mathcal{D}_3 \sinh(\beta_2 \Delta_2))\right.\\ &+ \left.\beta_2 \mathcal{D}_2 \left(\beta_3 \mathcal{D}_3 \cosh(\beta_2 \Delta_2) + \beta_2 \mathcal{D}_2 \sinh(\beta_2 \Delta_2)\right) \sinh(\beta_1 (\Delta_1 - z'))\right) &(18)\\ \text{denominator} &= \beta_2 \mathcal{D}_2 \cosh(\beta_2 \Delta_2) \left(\beta_1 (\mathcal{D}_1 + \beta_3 \mathcal{D}_3 z_0) \cosh(\beta_1 \Delta_1) + \left(\beta_3 \mathcal{D}_3 + \beta_1^2 \mathcal{D}_1 z_0\right) \sinh(\beta_1 \Delta_1)\right)\\ &+ \left(\beta_1 \left(\beta_3 \mathcal{D}_1 \mathcal{D}_3 + \beta_2^2 {\mathcal{D}_2}^2 z_0\right) \cosh(\beta_1 \Delta_1) + \left(\beta_2^2 {\mathcal{D}_2}^2 + \beta_1^2 \beta_3 \mathcal{D}_1 \mathcal{D}_3 z_0\right) \sinh(\beta_1 \Delta_1)\right)\\ &\times \sinh(\beta_2 \Delta_2) &(19) \end{aligned}$$

The field autocorrelation function $G_0(\boldsymbol{r}, \tau)$ measured at the position $\boldsymbol{r} = \{\boldsymbol{\rho}, z = 0\}$ on the surface of the medium is then obtained from the inverse Fourier transform

$$G_0(\boldsymbol{r}, \tau) = \frac{1}{2\pi} \int \mathrm{d}^2\boldsymbol{q}\, \hat{G}_0(\boldsymbol{q}, z = 0, \tau) e^{-i\boldsymbol{q}\boldsymbol{\rho}} \tag{20}$$

with respect to $\boldsymbol{q}$. In view of the complex form of the expressions, this transformation is performed numerically.

---

* Electronic address: `thomas.gisler@uni-konstanz.de`

[1] A. G. Yodh and B. Chance, Physics Today pp. 34–40 (1995).

[2] V. Tuchin, *Tissue Optics. Light Scattering Methods and Instruments for Medical Diagnosis*, vol. TT38 of *Tutorial Texts in Optical Engineering* (SPIE Press, Bellingham, WA, 2000).

[3] B. Chance, Ann. Acad. Sci. NY **838**, 29 (1998).

[4] N. P. Barry, M. J. Cole, M. J. Dayel, K. Dowling, P. M. W. French, S. C. W. Hyde, R. Jones, D. Parsons-Karavassilis, M. Tziraki, M. J. Lever, et al., in *Waves and Imaging through Complex Media*, edited by P. Sebbah (Kluwer, Dordrecht, 2001), pp. 213–234.

[5] J. M. Schmitt, A. Knüttel, and R. F. Bonner, Appl. Opt. **32**, 6032 (1993).

[6] D. A. Boas, M. A. O'Leary, B. Chance, and A. G. Yodh, Phys. Rev. E **47**, R2999 (1993).

[7] S. R. Arridge and M. Schweiger, Phil. Trans. R. Soc. Lond. B **352**, 717 (1997).

[8] M. A. Franceschini, V. Toronov, M. Filiaci, E. Gratton, and S. Fantini, Opt. Expr. **6**, 49 (2000).

[9] M. A. Franceschini, S. Fantini, J. J. Thompson, J. P. Culver, and D. A. Boas, Psychophysiol. **40**, 548 (2003).

[10] M. Wolf, U. Wolf, V. Toronov, A. Michalos, L. A. Paunescu, J. H. Choi, and E. Gratton, NeuroImage **16**, 704 (2002).

[11] G. Gratton, P. M. Corballis, E. Cho, M. Fabiani, and D. C. Hood, Psychophysiol. **32**, 505 (1995).

[12] M. Wolf, U. Wolf, H. J. Choi, R. Gupta, L. P. Safanova, L. A. Paunescu, A. Michalos, and E. Gratton, NeuroImage **17**, 1868 (2002).

[13] A. Grinvald, E. Lieke, R. D. Frostig, C. D. Gilbert, and T. N. Wiesel, Nature **324**, 361 (1986).

[14] A. Grinvald, L. Anglister, J. A. Freeman, R. Hildesheim, and A. Manker, Nature **308**, 848 (1984).

[15] L. B. Cohen, R. D. Keynes, and B. Hille, Nature **218**, 438 (1968).

[16] R. A. Stepnoski, A. LaPorta, F. Raccuia-Behling, G. E. Blonder, R. E. Slusher, and D. Kleinfeld, Proc. Natl. Acad. Sci. USA **88**, 9382 (1991).

[17] M. Heckmeier and G. Maret, Europhys. Lett. **34**, 257 (1996).

[18] M. Heckmeier, S. E. Skipetrov, G. Maret, and R. Maynard, J. Opt. Soc. Am. A **14**, 185 (1997).

[19] D. A. Boas, L. E. Campbell, and A. G. Yodh, Phys. Rev. Lett. **75**, 1855 (1995).

[20] G. Maret and P. E. Wolf, Z. Phys. B **65**, 409 (1987).

[21] D. J. Pine, D. A. Weitz, P. M. Chaikin, and E. Herbolzheimer, Phys. Rev. Lett. **60**, 1134

(1988).

[22] D. A. Weitz, D. J. Pine, P. N. Pusey, and R. J. A. Tough, Phys. Rev. Lett. **63**, 1747 (1989).

[23] X.-L. Wu, D. J. Pine, P. M. Chaikin, J. P. Huang, and D. A. Weitz, J. Opt. Soc. Am. B **7**, 15 (1990).

[24] D. Bicout and R. Maynard, Physica A **199**, 387 (1993).

[25] D. Bicout and G. Maret, Physica A **210**, 87 (1994).

[26] R. Lohwasser and G. Soelkner, Appl. Opt. **38**, 2128 (1999).

[27] A. K. Dunn, H. Bolay, M. A. Moskowitz, and D. A. Boas, J. Cereb. Blood Flow Metab. **21**, 195 (2001).

[28] C. Cheung, J. P. Culver, K. Takahashi, J. H. Greenberg, and A. G. Yodh, Phys. Med. Biol. **46**, 2053 (2001).

[29] S. E. Skipetrov and R. Maynard, Phys. Lett. A **217**, 181 (1996).

[30] D. B. Sattelle, D. J. Green, and K. H. Langley, Biol. Bull. **149**, 445 (1975).

[31] D. B. Sattelle, J. Exp. Biol. **139**, 233 (1988).

[32] D. Englert and C. Edwards, Proc. Natl. Acad. Sci. USA **74**, 5759 (1977).

[33] E. R. Kandel, J. H. Schwartz, and T. M. Jessell, *Principles of Neural Science* (McGraw-Hill, 2000), 4th ed.

[34] G. W. Goerres, M. Samuel, I. H. Jenkins, and D. J. Brooks, NeuroReport **9**, 3631 (1998).

[35] L. C. Hartlage and R. Gage, Neuropsych. Rev. **7**, 143 (1997).

[36] B. Kolb and I. Q. Whishaw, *Fundamentals of Human Neuropsychology* (Freeman, San Francisco, 2002), 5th ed.

[37] F. G. Andres and C. Gerloff, J. Clin. Neurophysiol. **16**, 520 (1999).

[38] R. Oldfield, Neuropsychol. **9**, 97 (1971).

[39] T. Gisler, H. Rüger, S. U. Egelhaaf, J. Tschumi, P. Schurtenberger, and J. Rička, Appl. Opt. **34**, 3546 (1995).

[40] Deutsche Industrie-Norm EN 60825-1, Deutsches Institut f. Normung e. V. (2003).

[41] H. H. Jasper, Electroencephal. Clin. Neurophysiol. **10**, 370 (1958).

[42] I. Flammer and J. Rička, Appl. Opt. **36**, 7508 (1997).

[43] B. J. Berne and R. Pecora, *Dynamic Light Scattering* (Krieger, Malabar, 1990).

[44] S. J. Matcher, M. Cope, and D. T. Delpy, Appl. Opt. **36**, 386 (1997).

[45] E. Okada, M. Firbank, M. Schweiger, S. R. Arridge, M. Cope, and D. T. Delpy, Appl. Opt.

36, 21 (1997).

[46] D. A. Boas, J. P. Culver, J. J. Stott, and A. K. Dunn, Opt. Expr. **10**, 159 (2002).

[47] G. Gratton and P. M. Corballis, Psychophysiol. **32**, 292 (1996).

[48] J. E. W. Mayhew, S. Askew, Y. Zheng, J. Porrill, G. W. M. Westby, P. Redgrave, D. M. Rector, and R. M. Harper, NeuroImage **4**, 183 (1996).

[49] K. Schätzel, Opt. Acta **30**, 155 (1983).

[50] M. Junghöfer, M. Bradley, T. Elbert, and P. Lang, Psychophysiol. **38**, 175 (2001).

[51] J. H. Choi, M. Wolf, V. Toronov, U. Wolf, C. Polzonetti, D. Hueber, L. P. Safonova, R. Gupta, A. Michalos, W. Mantulin, et al., J. Biomed. Opt. **9**, 221 (2004).

[52] We use $\overline{\tau} = \int_{\tau=200\,\mathrm{ns}}^{\tau=3.1\,\mathrm{s}} \mathrm{d}\tau\, (g^{(2)}(\tau) - 1)/\beta_{\mathrm{coh}}$.

[53] This value of β_{coh} results from a combination of the optics of the receiver fiber guiding 6 transverse modes, and the presence of about 2 longitudinal laser modes of unequal amplitude, yielding an effective mode number of $2 \times 6 = 12 \approx 1/\beta_{\mathrm{coh}}$.